

Step-edge-guided nucleation and growth mode transition of α-Ga_2O_3 heteroepitaxy on vicinal sapphire

Jinggang Hao(郝景刚), Yanfang Zhang(张彦芳), Yijun Zhang(张贻俊), Ke Xu(徐科), Genquan Han(韩根全), and Jiandong Ye(叶建东)

Citation: Chin. Phys. B, 2024, 33 (**8**): 086104. DOI: 10.1088/1674-1056/ad4ff6

What follows is a list of articles you may be interested in

Surface structure modification of $ReSe_2$ nanosheets via carbon ion irradiation

Mei Qiao(乔梅), Tie-Jun Wang(王铁军), Yong Liu(刘泳), Tao Liu(刘涛), Shan Liu(刘珊), and Shi-Cai Xu(许士才)
Chin. Phys. B, 2023, 32 (**2**): 026101. DOI: 10.1088/1674-1056/ac7297

Heterogeneous integration of GaSb layer on (100) Si substrate by ion-slicing technique

Ren-Jie Liu(刘仁杰), Jia-Jie Lin(林家杰), Zheng-Hao Shen(沈正皓), Jia-Liang Sun(孙嘉良), Tian-Gui You(游天桂), Jin Li(李进), Min Liao(廖敏), and Yi-Chun Zhou(周益春)
Chin. Phys. B, 2022, 31 (**7**): 076103. DOI: 10.1088/1674-1056/ac5605

Zn-Cu-codoped SnO_2 nanoparticles:Structural, optical, and ferromagnetic behaviors

Syed Zulfiqar, Zainab Iqbal, Jianguo Lü(吕建国)
Chin. Phys. B, 2017, 26 (**12**): 126104. DOI: 10.1088/1674-1056/26/12/126104

Microstructure evolution of Cu atomic islands on liquid surfaces in the ambient atmosphere

Zhang Xiao-Fei (张晓飞), Chen Hang (陈杭), Yu Sen-Jiang (余森江)
Chin. Phys. B, 2015, 24 (**7**): 076103. DOI: 10.1088/1674-1056/24/7/076103

Micro-track structure analysis for 100 MeV Si ions in CR-39 by using atomic force microscopy

Fang Mei-Hua (方美华), Wei Zhi-Yong (魏志勇), Zhang Zi-Xia (张紫霞), Zhu Li (朱立), Fu Yu (府宇), Shi Miao (石苗), Li Guang-Wu (黎光武), Guo Gang (郭刚)
Chin. Phys. B, 2013, 22 (**11**): 116105. DOI: 10.1088/1674-1056/22/11/116105

Step-edge-guided nucleation and growth mode transition of α-Ga_2O_3 heteroepitaxy on vicinal sapphire

Jinggang Hao(郝景刚)[1,2], Yanfang Zhang(张彦芳)[2,3], Yijun Zhang(张贻俊)[2], Ke Xu(徐科)[1,5,†], Genquan Han(韩根全)[4,5,‡], and Jiandong Ye(叶建东)[2,§]

[1] *Test & Analysis Platform, Suzhou Institute of Nano-Tech and Nano-Bionics, Chinese Academy of Sciences, Suzhou* 215123, *China*
[2] *School of Electronic Science and Engineering, Nanjing University, Nanjing* 210023, *China*
[3] *Wuxi Institute of Technology, Wuxi* 214121, *China*
[4] *School of Microelectronics, Xidian University, Xi'an* 710071, *China*
[5] *Suzhou National Laboratory for Materials Science, Jiangsu Institute of Advanced Semiconductors, Suzhou* 215123, *China*

(Received 8 April 2024; revised manuscript received 21 May 2024; accepted manuscript online 24 May 2024)

Controlling the epitaxial growth mode of semiconductor layers is crucial for optimizing material properties and device performance. In this work, the growth mode of α-Ga_2O_3 heteroepitaxial layers was modulated by tuning miscut angles (θ) from 0° to 7° off the $(10\bar{1}0)$ direction of sapphire (0002) substrate. On flat sapphire surfaces, the growth undergoes a typical three-dimensional (3D) growth mode due to the random nucleation on wide substrate terraces, as evidenced by the hillock morphology and high dislocation densities. As the miscut angle increases to $\theta = 5°$, the terrace width of sapphire substrate is comparable to the distance between neighboring nuclei, and consequently, the nucleation is guided by terrace edges, which energetically facilitates the growth mode transition into the desirable two-dimensional (2D) coherent growth. Consequently, the mean surface roughness decreases to only 0.62 nm, accompanied by a significant reduction in screw and edge dislocations to 0.16×10^7 cm^{-2} and 3.58×10^9 cm^{-2}, respectively. However, the further increment of miscut angles to $\theta = 7°$ shrink the terrace width less than nucleation distance, and the step-bunching growth mode is dominant. In this circumstance, the misfit strain is released in the initial growth stage, resulting in surface morphology degradation and increased dislocation densities.

Keywords: growth mode, miscut angle, crystalline quality, surface morphology

PACS: 61.72.uj, 61.72.Bb, 68.35.Ct, 61.72.Ff **DOI:** 10.1088/1674-1056/ad4ff6

1. Introduction

Corundum-structured α-Ga_2O_3 has emerged as a versatile material for developing power electronic devices, attributed to its predicted high breakdown field endowed by its large bandgap of 5.3 eV and favorable growth characteristics that are absent in the thermodynamically stable β-Ga_2O_3 polymorph.[1–4] Device-oriented implementations based on α-Ga_2O_3, such as solar-blind photodetectors with high photoresponsivity and specific detectivity,[5–8] Schottky barrier power diodes with an ultra-low specific on-resistance, and enhanced heat dissipation capabilities,[9] have been demonstrated. Despite of these promising advantages, α-Ga_2O_3 can be only achieved on foreign substrates due to its metastable nature, and the misfit strain leads to much higher threading dislocation densities than those in β-Ga_2O_3 homoepitaxial layer.[10–12] These harmful defects typically result in significant carrier compensation and mobility degradation, inevitably leading to an increase in reverse leakage current and premature power device breakdown.[9,13–16]

Owing to the significant potential of α-Ga_2O_3 as previously noted, various growth equation methods have been employed for heteroepitaxial growth of α-Ga_2O_3 on sapphire substrates, including halide vapor phase epitaxy (HVPE), metal–organic chemical vapor deposition (MOCVD), molecular beam epitaxy (MBE), metal–organic vapor phase epitaxy (MOVPE), and mist chemical vapor deposition (Mist-CVD). Among these, Mist-CVD stands out for its non-vacuum, cost-effective nature in semiconductor epitaxial growth. Drawing on the chemical reaction principles akin to MOCVD and ALD, Mist-CVD technique employs water as an oxygen source, which is particularly suited for fabricating epitaxial oxide layers such as ZnO, CrO, CuO, In_2O_3, SnO_x,[17–21] etc. Recent advancements in gallium oxide synthesis via Mist-CVD encompass large-scale epitaxy, alloy epitaxial layers, n-type doping, power devices, and others. Moreover, p-type oxides like NiO and LiGaO[22–27] can be prepared using Mist-CVD. This technique is anticipated to significantly influence the field of semiconductor epitaxial layer synthesis, especially for oxide-based semiconductors. However, the current α-Ga_2O_3 epilayers on sapphire substrates grown by Mist-CVD exhibit issues that require resolution, specifically concerning inferior surface morphology and elevated dislocation densities.

To date, substantial endeavors have been undertaken to reduce dislocation densities in lattice-mismatched α-Ga_2O_3

†Corresponding author. E-mail: kxu2006@sinano.ac.cn
‡Corresponding author. E-mail: gqhan@xidian.edu.cn
§Corresponding author. E-mail: yejd@nju.edu.cn

© 2024 Chinese Physical Society and IOP Publishing Ltd

epilayers.[28] This has been achieved through approaches such as increasing the epitaxial thickness or utilizing epitaxial lateral overgrowth techniques.[29] The dislocation evolution in α-Ga_2O_3 heteroepitaxial layer strongly depend on the initial heterogeneous nucleation mechanism and the subsequent epitaxial mode, where the formation energy and the evolution of misfit strain play decisive roles.[30–32] Sapphire (α-Al_2O_3) is commonly chosen as the substrate for α-Ga_2O_3 epitaxy due to the identical corundum structure. However, the in-plane lattice mismatch of 4.81% and thermal expansion coefficient mismatch (about 20%) between α-Ga_2O_3 and α-Al_2O_3 typically result in granular structures with edge dislocation densities as high as 10^{11} cm^{-3} and a rough surface morphology.[33] As demonstrated in the growth of GaN on misoriented sapphire substrates, manipulation of misfit strain energy by adjusting the dimensions of surface step terraces determines the initial nucleation mechanism and growth mode.[34,35] It is anticipated that the surface terraces of substrate with width comparable to the diffusion length of adatoms will facilitate efficient nucleation at terrace edges and promote the favorable 2D growth mode.[36–38] Although the heteroepitaxy of α-Ga_2O_3 on misoriented substrates has been demonstrated, the correlation between the nucleation mechanism, growth mode and dislocation dynamics have not been well exploited. In this contribution, we present experimental evidences of step-edge-guided nucleation and growth mode transition of α-Ga_2O_3 heteroepitaxy on vicinal sapphire, along with an investigation into the associated evolution of dislocations and misfit strain.

2. Experiment and method

In this work, α-Ga_2O_3 heteroepitaxial layers were grown utilizing a hot-wall mist-CVD system on sapphire (0002) substrates with miscut angles from 0° to 7° off (10$\bar{1}$0) direction. The system configuration and growth details have been described in our previous work. Gallium acetylacetonate, employed as the Ga precursor, was dissolved in de-ionized water (0.05 mol/L) with 1.0% hydrochloric acid and atomized into micrometer-sized droplets using a 2.4-MHz ultrasonic transducer. High-purity O_2 carrier gas transported the precursors into the growth chamber at a flow rate of 750 sccm. The growth process was optimized at a temperature of 470 °C under atmospheric pressure, and the resultant α-Ga_2O_3 heteroepitaxial layers are approximately 3 μm in thickness. High-resolution x-ray diffraction (HRXRD) measurements were performed using a D8 diffractometer equipped with a Cu $K\alpha1$ (1.54056 Å) line and a Ge (004) channel-cut crystal with a high resolution of 0.0001°. The surface morphology was characterized by scanning electron microscopy (SEM, Gemini 500) and atomic force microscopy (AFM) operated in a tapping mode. High-resolution transmission electron microscopy (HRTEM) was performed using a monochromator FEI Titan STEM operated at 200 kV.

3. Results and discussion

The surface diffusion phenomena play a significant role in determining the crystalline quality and surface morphology of α-Ga_2O_3 epilayers grown on sapphire substrates. The growth mode of α-Ga_2O_3 heteroepitaxial layer is closely related to the surface morphology, which is influenced by the Ga surface diffusion phenomena.[39–41] In this study, AFM measurements were conducted on α-Ga_2O_3 epilayers grown on sapphire substrates with miscut angles ranging from 0° to 7° (as depicted in Fig. 1). The miscut angle of the substrate was found to have an impact on the Ga surface diffusion phenomena. The researchers investigated the growth mode of α-Ga_2O_3 heteroepitaxial layers by modulating the miscut angle off *A*-axis direction of *C*-plane sapphire substrate. To discuss the effect of growth mode on surface morphology and crystalline quality of α-Ga_2O_3 heteroepitaxial layers on sapphire substrates with different miscut angles, we summarized the main experimental observations and discussed the underlying physical mechanisms.

Generally, the growth mode of hetero-epilayers is mirrored by the surface morphology. The growth mode of α-Ga_2O_3 epitaxial layers on substrates is determined by the relative magnitude of the terrace width and the distance between neighboring nuclei, rather than the surface diffusion length of Ga. Figure 1 illustrates the AFM morphologies of α-Ga_2O_3 epilayers on sapphire substrates with varied miscut angles. As shown in Fig. 1(a), where $\theta = 0°$, the terrace width d of sapphire substrate approach infinity, significantly larger than the distance between neighboring nuclei r_0. Under this circumstance, nucleation would occur, leading to the growth mode of 3D islands. The AFM image in Fig. 1(a) depicts islands with large diameters and root-mean-square (RMS) roughness of 40.59 nm. When $\theta = 3°/4°$, the terrace width d calculated as 14.83 nm/11.12 nm on vicinal surfaces is slightly larger than the distance between neighboring nuclei near the steps, nucleation would also occur in this case. Atomic steps on vicinal surfaces would serve as nucleation sites, with gallium atoms adsorbed at the steps initiating the transition to the epitaxy process of step-flow growth mode. The 3D islands would merge resulting in a larger diameter and smaller fluctuation of the islands, as displayed in AFM images of Figs. 1(b) and 1(c), caused by the 3D islands/step-flow multiple growth mode. At θ =3°, the surface of α-Ga_2O_3 heteroepitaxial layer appears relatively flat without obvious 3D islands, with the RMS significantly reduced to 2.01 nm due to the transformation of growth mode. At $\theta = 4°$, epitaxial fringes alone in the [11$\bar{2}$0] direction on the α-Ga_2O_3 heteroepitaxial layer are observed, further reducing the RMS to 1.53 nm.

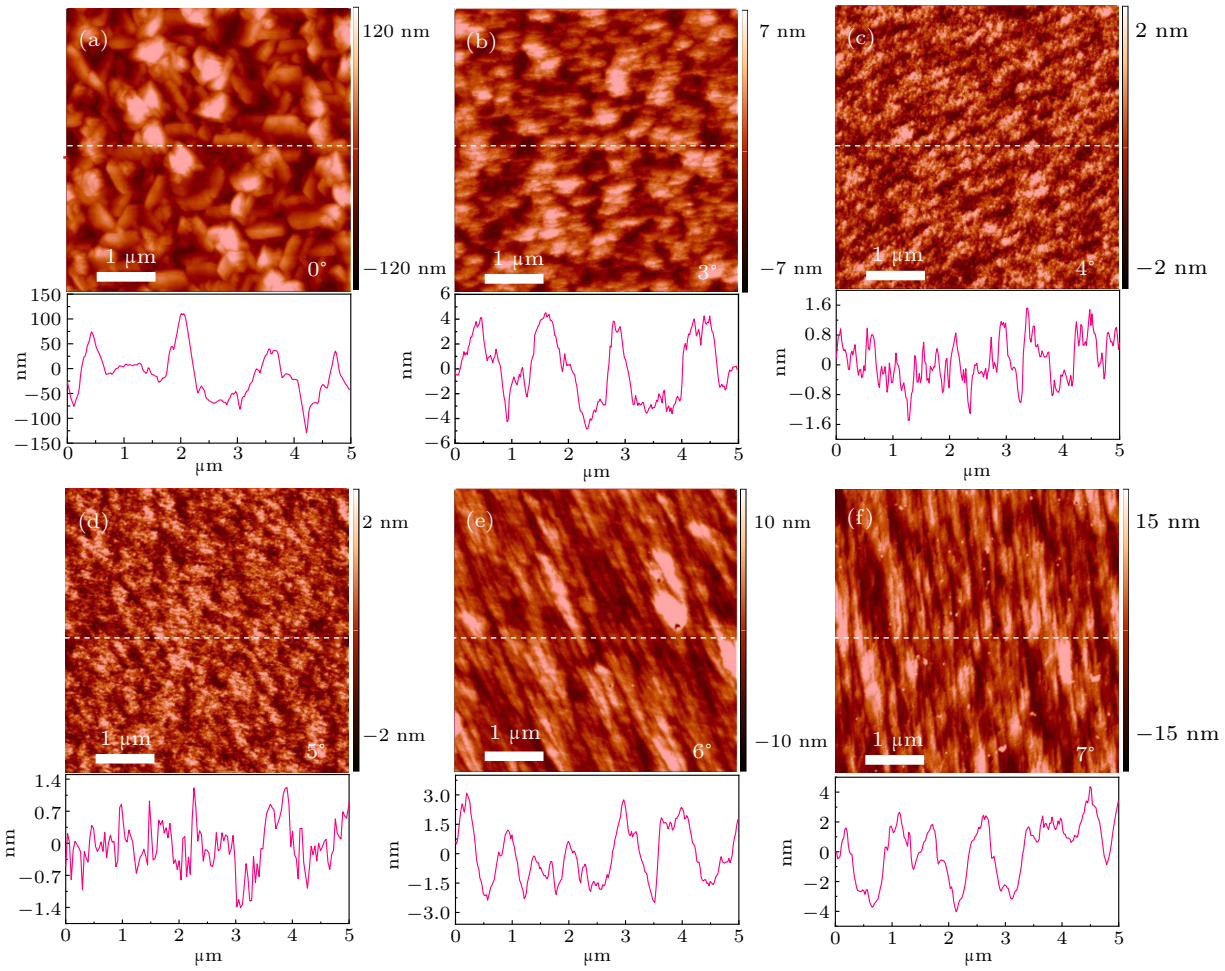


Fig. 1. AFM images and line-profiles of α-Ga_2O_3 epilayers on sapphire substrate with miscut angles of (a) 0°, (b) 3°, (c) 4°, (d) 5°, (e) 6°, (f) 7°.

As θ increases to 5°, the terrace width (d) of 8.65 nm approaches the distance between neighboring nuclei. With increasing miscut angle, step meandering and ultimately stepflow growth mode take place, resulting in α-Ga_2O_3 heteroepitaxial layers with high crystalline perfection and ameliorative morphology. The surface morphology of the α-Ga_2O_3 heteroepitaxial layer has been ameliorated significantly without obvious granular structures and the RMS reduced to 0.62 nm as shown in the AFM image of Fig. 1(d). With further increase of θ to 6°/7°, the terrace width d of 7.42 nm/6.18 nm is to a certain extent less than the distance between neighboring nuclei, leading to a transition to step-bunching growth mode. At $\theta = 6°$, well-aligned epitaxial fringes alone $[11\bar{2}0]$ direction on the α-Ga_2O_3 heteroepitaxial layer were present, which were created by anisotropic epitaxial growth, triggered by the step-bunching growth mode with a slightly increasing RMS of 1.91 nm as seen in Fig. 1(e), and α-Ga_2O_3 granules appear on the epitaxial fringes. At θ =7°, aligned epitaxial fringes along the $[11\bar{2}0]$ direction on α-Ga_2O_3 heteroepitaxial layer become closer as the terrace width decreases, and the RMS increases to 2.41 nm as seen in Fig. 1(f), with a slight increase in α-Ga_2O_3 granules on the epitaxial fringes.

The extracted line profiles and their corresponding height data are graphically represented in Fig. 1, requiring thorough analysis and discussion. When $\theta = 0°$, as depicted in Fig. 1(a), the line-profiles exhibit substantial undulations spanning −120 nm to 120 nm, signifying the emergence of distinct 3D islands on the sample surface. This topographical feature arises from the 3D island growth mode, which engenders the development of these elevated formations. When $\theta = 3°$, the line-profiles become notably smoother, oscillating within the range of −5 nm to 5 nm, a phenomenon attributable to the the 3D islands/step-flow multiple growth mode, which results in the flattening of the 3D islands on the sample surface, corroborated by the AFM image presented in Fig. 1(b). When $\theta = 4°$, upon scrutinizing Fig. 1(c), the line-profiles' oscillations are further attenuated, constrained within the −1.5 nm to 1.5 nm span. When $\theta = 5°$, under the influence of step-flow growth, the line-profiles manifest a pronouncedly subdued undulation, with fluctuations restricted to the −1 nm to 1 nm band. This discernment reflects a considerable diminution in surface roughness, evincing a more uniform and planar surface configuration, as illustrated in Fig. 1(d). With a further escalation of θ to 6°, the α-Ga_2O_3 heteroepitaxial layer exhibits aligned epitaxial fringes and gently undulating islands, ascribed to the step-bunching growth mode, which broadens

the oscillation span of the line-profiles to a range of −3 nm to 3 nm, as shown in Fig. 1(e). When $\theta = 7°$, the aligned epitaxial fringes become more pronounced and the undulations of the islands intensify, the oscillation range of the line-profiles expands to span from −4 nm to 4 nm, as presented in Fig. 1(f). The line-profiles variations correlate with AFM images shown in Fig. 1 and the values of RMS shown in Fig. 2(c), signifying alterations in the growth mode of α-Ga_2O_3 epilayers on sapphire substrates with different miscut angles.

High-resolution x-ray diffraction (XRD) patterns of α-Ga_2O_3 epilayers on sapphire substrates with varying miscut angles are depicted in Fig. 2(a). These patterns confirm the successful growth of single-crystal α-Ga_2O_3 epilayers on sapphire substrates with different miscut angles. The lattice mismatch between α-Ga_2O_3 and α-Al_2O_3 would lead to the generation of threading dislocations and lattice distortion for specific crystallographic planes due to the residual stress in epitaxial layers.[42,43] The x-ray rocking curves (XRC) were conducted for different samples under both symmetric and skew symmetric geometries, focusing on the (0006) and $(10\bar{1}4)$ planes of α-Ga_2O_3 epilayers on sapphire substrates with miscut angles ranging from 0° to 7°. The full width at half maximum (FWHM) value was extracted and displayed in Fig. 2(b). A mosaic model has been employed to explore dislocation density in epitaxial layers, treating the layer as a collection of smaller, tilted mosaics. Each mosaic is linked to a dislocation that causes its tilt relative to neighboring mosaics. The orientations of these mosaics are presumed to follow a Gaussian distribution, offering a method to assess dislocation density in the epitaxial structure. In 1953, Gay introduced a formula $D_B = \beta/3st$ when researching the total dislocation densities within the particles and the densities in annealed metals from x-ray diffraction photographs. Here D_B is the density of dislocations in the boundaries, β represents the angular spread of particles in the original grain identified by the half-width of the Gaussian distribution curve, t is the spacing between subgrain boundaries and s is the Burgers vector.[44] In 1957, Dunn and Koch refined the formula to $\rho = \beta^2/(2\pi \ln 2b^2) = \beta^2/(4.35b^2)$ where ρ is the dislocation density, assuming a Gaussian distribution for the subgrain orientations with a half-width of β and b is Burgers vector.[45] In 1999, Heinke analyzed edge and screw dislocation densities in GaN epitaxial layers using the model.[46] Kaganer (2005) and subsequent researchers adopted more direct approaches to assess these densities: $D_s = \beta^2/(2\pi \ln 2)b_s^2$ and $D_e = \beta^2/(2\pi \ln 2)b_e^2$, where D_e (D_s) and b_e (b_s) are dislocation densities and lengths of Burgers vectors for edge (screw) types, respectively.[47–49] For α-Ga_2O_3, the Burgers vectors are denoted by $b_e = \frac{1}{3}\langle 2\bar{1}\,\bar{1}0\rangle$ and $b_s = \langle 0001\rangle$, the corresponding screw and edge dislocation densities were calculated and particularized in Fig. 2(c).

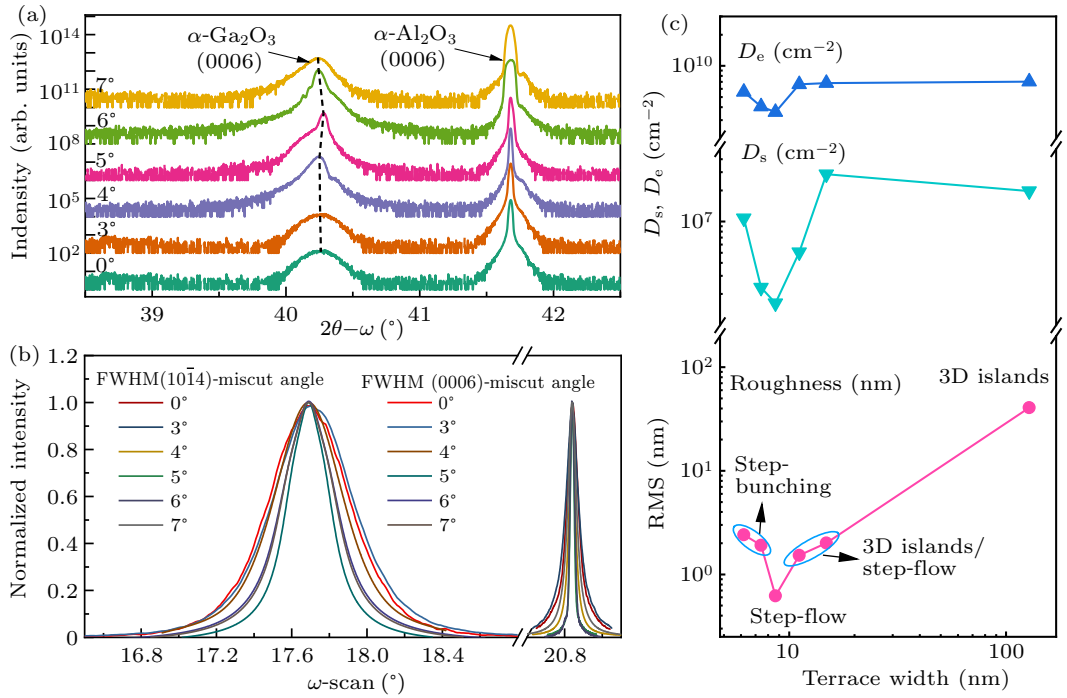


Fig. 2. (a) XRD 2θ–ω scan patterns of α-Ga_2O_3 epilayers on sapphire substrate with different miscut angles, (b) FWHM of (0006) and (10$\bar{1}$4) planes of the α-Ga_2O_3 epilayers, (c) screw dislocation density, edge dislocation density, and RMS of the α-Ga_2O_3 epilayers.

As shown in Fig. 2(c), when $\theta = 0°$, high screw and edge dislocation densities in the α-Ga_2O_3 heteroepitaxial layer were measured at 1.97×10^7 cm^{-2} and 7.05×10^9 cm^{-2}, consistent with the TEM images shown in Figs. 3(a) and 3(b). This elevated dislocation density is attributed to the presence of numerous grain boundaries caused by the 3D islands growth mode. When $\theta = 3°$, the screw and edge dislocation densities of α-Ga_2O_3 heteroepitaxial layer was 2.86×10^7 and

6.83×10^9 cm^{-2} obtained by calculation according to Fig. 2(c), profiting from the 3D islands/step-flow multiple growth mode. When $\theta = 4°$, The screw and edge dislocation densities of α-Ga_2O_3 heteroepitaxial layer reduced to 0.51×10^7 cm^{-2} and 6.65×10^9 cm^{-2}, due to the larger proportion of the step-flow growth mode. When $\theta = 5°$, the screw and edge dislocation densities of α-Ga_2O_3 heteroepitaxial layer reduced to 0.16×10^7 cm^{-2} and 3.58×10^9 cm^{-2}, in line with the TEM images shown in Figs. 3(f) and 3(g). The screw dislocation density was 91% and the edge dislocation density was 49% lower than that on flat surfaces of sapphire substrates benefited by a depressed grain boundary density. When $\theta = 6°$, The screw and edge dislocation densities of α-Ga_2O_3 heteroepitaxial layer increased to 0.23×10^7 cm^{-2} and 4.05×10^9 cm^{-2}, indicating an augmented grain boundary density evocable via the step-bunching growth mode. When $\theta = 7°$, the screw and edge dislocation densities of α-Ga_2O_3 heteroepitaxial layer increased ulteriorly to 1.08×10^7 cm^{-2} and 5.62×10^9 cm^{-2}, as the prominence of the step-bunching growth mode intensified.

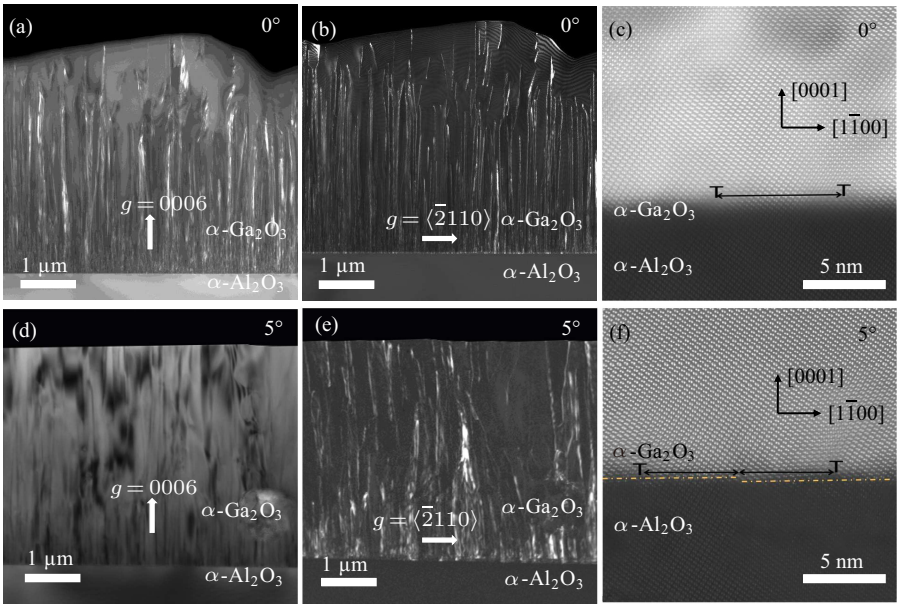


Fig. 3. TEM images of α-Ga_2O_3 epilayers. TEM images of α-Ga_2O_3 epilayer with diffraction vectors of $g = \langle0006\rangle$ and $\langle\bar{2}110\rangle$ on sapphire substrate with 0° [panels (a) and (b)] and 5° [panels (d)–(e)] miscut angles, STEM images of α-Ga_2O_3 epilayers on sapphire substrate with 0° (c) and 5° (f) miscut angles.

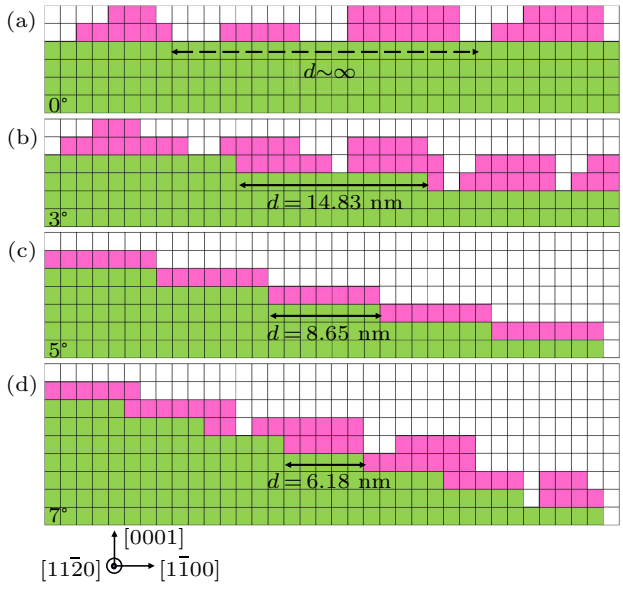


Fig. 4. Schematic diagram of the transformation of growth mode of α-Ga_2O_3 epilayers on sapphire substrate with different miscut angles.

Rough surface and large dislocation density of α-Ga_2O_3 epilayers were obtained on flat sapphire substrates. The growth predominantly exhibited typical 3D modes due to random nucleation on wide terraces, as evidenced by distinctive hillock morphology and elevated dislocation densities. Profited from the transformation of growth mode into 3D islands/step-flow multiple growth mode, the crystalline quality and surface morphology of α-Ga_2O_3 epilayers on sapphire substrates with miscut angles of $3°/4°$ have been significantly improved than those on flat substrates. When θ increases, atomically smooth surface and significantly reduced dislocation density of α-Ga_2O_3 single crystalline epilayers were achieved at $\theta = 5°$, benefiting from the step-flow growth mode. Deteriorative surface morphology and crystal quality would appear in α-Ga_2O_3 epilayers, when θ increases further to $6°/7°$, and the growth mode would gonna become to step-bunching.

In settled growth conditions on a vicinal surface, the quantitative value r_s of the distance between neighboring 3D nuclei is constant, while the terrace width d varies with different substrate miscut angles.[50] With the miscut angles increasing, growth mode of 3D islands, 3D islands/step-flow, step-flow, and step-bunching alternated in turn. The transformation

of growth mode of the α-Ga_2O_3 heteroepitaxial layers caused by different miscut angles of sapphire substrate was demonstrated in Fig. 4.[51] It is shown that 3D islands growth mode would occur on flat surfaces of sapphire substrates and high dislocation density and rough surface of α-Ga_2O_3 heteroepitaxial layers would be obtained. The surface diffusion length λ has a relation not only to the terrace widths on the vicinal surfaces, but also to the sticking coefficient of adatoms to the atomic steps.[50]

Interactions between growth models and dislocations in α-Ga_2O_3 heteroepitaxial layers warrant discussion. As the miscut angle $\theta = 5°$, the screw dislocation density was more than an order of magnitude and edge dislocation density about half lower than that on flat surfaces of sapphire substrates. One contributing factor was the reduced grain boundary density resulting from the step-flow growth mode. When $\theta = 0°$, at the interface along the $[1\bar{1}00]$ axis, periodic structures with a spacing of 8.65 nm were observed in the STEM image Fig. 3(c), corresponding to the matching of 20 α-Ga_2O_3 cells and 21 α-Al_2O_3 cells.[52] The lattice mismatches between α-Ga_2O_3 epilayer and α-Al_2O_3 substrate were the main reason for the large dislocation density in α-Ga_2O_3 heteroepitaxial layer. When $\theta = 5°$, the mismatch sites between α-Ga_2O_3 epilayer and α-Al_2O_3 substrates would appear at the middle and the joint of the atomic steps found in the STEM image Fig. 3(f), which were convenient for the fusion and annihilation of dislocations leading to a decreasing dislocation density.

Another reason for the reduced dislocation density was the storage of strain energy between the epilayers and vicinal substrates, as evidenced by the high-resolution XRD 2θ–ω patterns of the α-Ga_2O_3 epilayers shown in Fig. 2(a) and the strain pictures shown in Fig. 5. From the XRD 2θ–ω patterns in Fig. 2(a), it can be observed that the peak of α-Ga_2O_3 epilayers on sapphire substrates with miscut angles of 4°, 5°, and 6° distinctly shifted to the right ($\theta = 5°$ especially), indicating the presence of residual compressive stress in the α-Ga_2O_3 epilayers. As shown in the ε_{xx} and ε_{yy} mappings from the GPA analysis of $[1\bar{1}00]$ zone axis STEM images of α-Ga_2O_3 epilayers on sapphire substrates with miscut angle of 0° in Figs. 5(a)–5(d) and 5° in Figs. 5(e)–5(h), the residual stress containing in the α-Ga_2O_3 epilayer on sapphire substrate with miscut angle of 5° is significantly greater than that of 0°.[53] Due to the stress release process, an increase in dislocation density occurs, explaining why the α-Ga_2O_3 epilayer on the sapphire substrate with a miscut angle of 5° exhibits the lowest dislocation density. From the TEM images of α-Ga_2O_3 epilayers on sapphire substrate with miscut angles of 0° in Figs. 3(a)–3(b) and 5° in Figs. 3(d)–3(e), it can be discovered that the dislocation density of α-Ga_2O_3 epilayer on sapphire substrate with miscut angle of 5° is significantly lower than that of 0°, which is consistent with the residual stress theory analysed above.

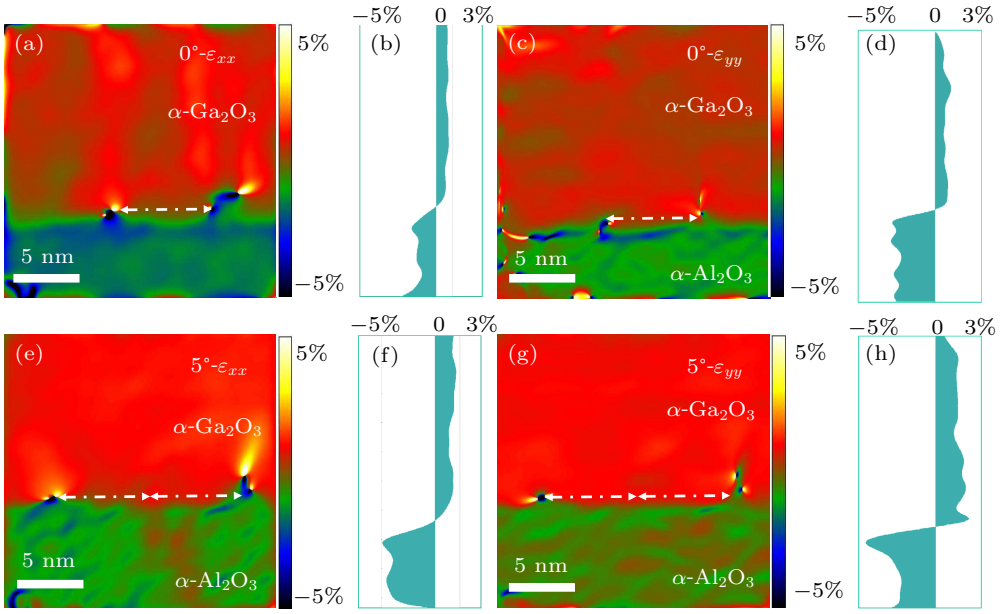


Fig. 5. The ε_{xx} and ε_{yy} mappings from the GPA analysis of $[1\bar{1}00]$ zone axis STEM images of α-Ga_2O_3 epilayers on sapphire substrates with miscut angle of 0° in panels (a)–(d) and 5° in panels (e)–(h).

4. Conclusions

By deliberately modulating the growth mode on miscut *C*-plane sapphire substrate, α-Ga_2O_3 single crystalline epilayers with atomically smooth surface and reduced dislocation density were achieved. As the miscut angle (θ) increased, growth mode of 3D islands, 3D islands/step-flow, step-flow and step-bunching alternated in turn. When $\theta = 5°$, the terrace width (d) closely matched the distance between neighboring nuclei (r_s), facilitating the onset of the step-flow growth mode. At this optimal miscut angle, the root-mean-square

(RMS) roughness of the α-Ga_2O_3 heteroepitaxial layer was reduced to less than 1 nm, accompanied by a remarkable reduction in screw dislocation density by more than an order of magnitude, and a halving of the edge dislocation density compared to that on flat sapphire surfaces. This improvement underscores the efficacy of controlling the miscut angle to enhance the overall quality of α-Ga_2O_3 heteroepitaxial layers. Such enhanced epitaxial layers hold significant promise for diverse applications in semiconductor technology, where precise control over material quality is paramount for optimal device performance and reliability.

Data availability statement

The data that supports the findings of this study are available in the supplementary material.

Acknowledgements

Project supported by the National Key Research and Development Program of China (Grant No. 2022YFB3605403), the National Natural Science Foundation of China (Grant Nos. 62234007, 62241407, 62293521, 62304238, 62241407, U21A20503, and U21A2071), the Key-Area Research and Development Program of Guangdong Province, China (Grant No. 2020B010174002), and the Cultivation Project for Youth Teachers in Jiangsu Province, and Jiangsu Funding Program for Excellent Postdoctoral Talent.

References

[1] Waseem A, Ren Z J, Huang H C, Nguyen K, Wu X H and Li X L 2023 *Phys. Status Solidi A* **220** 2200616
[2] Biswas M and Nishinaka H 2022 *APL Mater.* **10** 060701
[3] Galazka Z 2022 *J. Appl. Phys.* **131** 031103
[4] Singh R, Lenka T R, Panda D K, Velpula R T, Jain B, Bui H Q T and Nguyen H P T 2020 *Mat. Sci. Semicon. Proc.* **119** 105216
[5] Sun X Y, Wang Z P, Gong H H, Chen X H, Zhang Y J, Wang Z Y, Yu X X, Ren F F, Lu H, Gu S L, Zheng Y D, Zhang R and Ye J D 2022 *IEEE Electron. Dev. Lett.* **43** 3156177
[6] Sun X Y, Chen X H, Hao J G, Wang Z P, Xu Y, Gong H H, Zhang Y J, Zhang R and Ye J D 2021 *Appl. Phys. Lett.* **119** 141601
[7] Xie C, Lu X T, Tong X W, Zhang Z X, Liang F X, Liang L and Wu Y C 2019 *Adv. Func. Mater.* **29** 1806006
[8] Xi Z Y, Yang L L, Shu L C, Zhang M L, Li S, Shi L, Liu Z, Guo Y F and Tang W H 2023 *Chin. Phys. B* **32** 088502
[9] Kaneko K, Fujita S and Hitora T 2018 *Jpn. J. Appl. Phys.* **57** 02CB18
[10] Kaneko K, Fujita S and Hitora T 2023 *Jpn. J. Appl. Phys.* **62** SF0803
[11] Vogt S, Petersen C, Knei M, Splith D, Schultz T, Wenckstern H, Koch N and Grundmann M 2023 *Phys. Status Solidi A* **220** 2200721
[12] Williams M S, Orts M A, Schowalter M, Karg A, Raghuvansy S, McCandless J P, Jena D, Rosenauer A, Eickhoff M and Vogt P 2024 *APL Mater.* **12** 011120
[13] Ahmadi E and Oshima Y 2019 *J. Appl. Phys.* **126** 160901
[14] Oshima Y and Ahmadi E 2022 *Appl. Phys. Lett.* **121** 260501
[15] Xie W L, Lv X Y, Wang Q L, Li L A and Zou G T 2022 *Chin. Phys. B* **31** 108106
[16] Köpp S, Petersen C, Splith D, Grundmann M and von Wenckstern H 2023 *J. Vac. Sci. Technol. A* **41** 043411
[17] Narin P, Kutlu-Narin E, Kayral S, Tulek R, Gokden S, Teke A and Lisesivdin S B 2022 *J. Lumin.* **251** 119158
[18] Dang G T, Suwa Y, Sakamoto M, Liu L, Rutthongjan P, Sato S, Yasuoka T, Hasegawa R and Kawaharamura T 2018 *Appl. Phys. Express* **11** 111101
[19] Watahiki T, Yuda Y, Furukawa A, Yamamuka M, Takiguchi Y and Miyajima S 2017 *Appl. Phys. Lett.* **111** 222104
[20] Kuang Y, Chen X H, Ma T C, Du Q Q, Zhang Y F, Hao J G, Ren F F, Liu B, Zhu S M, Gu S L, Zhang R, Zheng Y D and Ye J D 2021 *ACS Appl. Electron. Mater.* **3** 795
[21] Liu L, Uedab M and Kawaharamura T 2023 *RSC Adv.* **13** 13456
[22] Wang X J, Mu W X, Xie J H, Zhang J T, Li Y, Jia Z T and Tao X T 2023 *J. Semicond.* **44** 062803
[23] Uno K and Ohta M 2023 *Jpn. J. Appl. Phys.* **62** SF1026
[24] Wakamatsu T, Isobe Y, Takane H, Kaneko K and Tanaka K 2024 *J. Appl. Phys.* **135** 155705
[25] Liu Z, Li P G, Zhi Y S, Wang X L, Chu X L and Tang W H 2019 *Chin. Phys. B* **28** 017105
[26] Ikenoue T, Inoue J, Miyake M and Hirato T 2019 *J. Crystal Growth* **507** 379
[27] Zhang K T, Thirupakuzi Vangipuram V G, Huang H L, Hwang J and Zhao H P 2023 *Adv. Electron. Mater.* 2300550
[28] Jinno R, Uchida T, Kaneko K and Fujita S 2016 *Appl. Phys. Express* **9** 071101
[29] Zhang Y J, Wang Z P, Kuang Y, Gong H H, Hao J G, Sun X Y, Ren F F, Yang Y, Gu S L, Zheng Y D, Zhang R and Ye J D 2022 *Appl. Phys. Lett.* **120** 121601
[30] Fan Z Y and Men H 2022 *Metals* **12** 1547
[31] Jun Y S, Kim D and Neil C W 2016 *Acc. Chem. Res.* **49** 1681
[32] Hooks D E, Fritz T and Ward M D 2001 *Adv. Mater.* **13** 227
[33] Shinohara D and Fujita S 2008 *Jpn. J. Appl. Phys.* **47** 7311
[34] Huang X, Bai J, Dudley M, Dupuis R D and Chowdhury U 2005 *Appl. Phys. Lett.* **86** 211916
[35] Mukhopadhyay S, Sanyal S, Wang G, Gupta C and Pasayat S S 2023 *Crystals* **13** 1457
[36] Fu J H, Min J C, Chang C K, Tseng C C, Wang Q, Sugisaki H, Li C Y, Chang Y M, Alnami I, Syong W R, Lin C, Fang F, Zhao L, Lo T H, Lai C S, Chiu W S, Jian Z S, Chang W H, Lu Y J, Shih K M, Li L J, Wan Y, Shi Y M and Tung V 2023 *Nat. Nanotechnol.* **18** 1289
[37] Aruta C, Ricci F, Balestrino G, Lavanga S, Medaglia P G, Orgiani P, Tebano A and Zegenhagen J 2002 *Phys. Rev. B* **65** 195408
[38] Brinks P, Siemons W, Kleibeuker J E, Koster G, Rijnders G and Huijben M 2011 *Appl. Phys. Lett.* **98** 242904
[39] Bhuiyan A F M A U, Feng Z, Johnson J M, Huang H L, Hwang J and Zhao H P 2020 *Cryst. Growth Des.* **20** 6722
[40] Banal R G, Funato M and Kawakami Y 2009 *Phys. Status Solidi C* **6** 599
[41] Schewski R, Baldini M, Irmscher K, Fiedler A, Markurt T, Neuschulz B, Remmele T, Schulz T, Wagner G, Galazka Z and Albrecht M 2016 *J. Appl. Phys.* **120** 225308
[42] Smirnov A M, Kremleva A V, Sharofidinov S S, Bougrov V E and Romanov A E 2020 *Appl. Phys. Express* **13** 075502
[43] Son H and Jeon D W 2019 *J. Alloys Compd.* **773** 631
[44] Gay P, Hirsch P B and Kelly A 1953 *Acta Metall.* **1** 315
[45] Dunn C G and Kogh E F 1957 *Acta Metall.* **5** 548
[46] Heinke H, Kirchner V, Einfeldt S and Hommel D 1999 *Phys. Stat. Sol. (a)* **176** 391
[47] Kaganer V M, Brandt O, Trampert A and Ploog K H 2005 *Phys. Rev. B* **72** 045423
[48] Moram M A and Vickers M E 2009 *Rep. Prog. Phys.* **72** 036502
[49] Ma T C, Chen X H, Ren FF, Zhu S M, Gu S L, Zhang R, Zheng Y D and Ye J D 2019 *J. Semicond.* **40** 012804
[50] Hata M, Isu T, Watanabe A, Kajikawa Y and Katayama Y 1991 *J. Cryst. Growth* **114** 203
[51] Tokura Y, Saitos H and Fukui T 1989 *J. Cryst. Growth* **94** 46
[52] Kaneko K, Kawanowa H, Ito H and Fujita S 2012 *Jpn. J. Appl. Phys.* **51** 020201
[53] Kuang Y, Ma T C, Chen X H, Hao J G, Ren F F, Gu S L, Zhang R, Zheng Y D and Ye J D 2021 *Appl. Phys. Lett.* **119** 182102